

VIP Very Important Paper

www.batteries-supercaps.org

High-Coulombic-Efficiency Hard Carbon Anode Material for Practical Potassium-Ion Batteries

Lulu Tan,^[a, b] Jiale Chen,^[a] Linlin Wang,^[a] Nan Li,^[a] Yusi Yang,^[a] Yifan Chen,^[a] Lin Guo,^[a] Xiao Ji,^[c] and Yujie Zhu^{*[a]}

Biomass-derived hard carbon (HC) has emerged as a promising candidate for anode materials of potassium-ion batteries because of low cost and abundant raw materials. Whereas, the large specific surface area and high porosity of this type of HC often lead to inferior initial Coulombic efficiency (ICE) and unsatisfactory cycling stability. Herein, we report a coconut shell-derived HC (CS-HC) featuring an expanded interlayer spacing and small specific surface area. The CS-HC delivers a reversible specific capacity of 280 mAh g⁻¹ and an impressive ICE of 87.32% at 50 mA g⁻¹. In addition, it exhibits stable cycling performance (92.8% capacity retention after 100 cycles at 50 mA g⁻¹) and fast rate capability (~280 mAh g⁻¹ at

300 mA g⁻¹). The *ex situ* Raman spectra characterization combined with cyclic voltammetry tests elucidate that the storage of potassium ions in the present HC is mainly achieved by (pseudo)capacitive behavior at the disordered defect sites along with minor contribution from the interlayer intercalation process. Finally, a full-cell constructed with unrecycled CS-HC anode and high-voltage K₂Mn[Fe(CN)₆] cathode demonstrates exceptional electrochemical stability and retains 90.6% capacity after 100 cycles. This work reports a high-performance HC anode material derived from low-cost and sustainable biomass for practical potassium-ion batteries.

Introduction

Lithium-ion batteries (LIBs) are confronted with the increasing anxiety on the limited reserve, uneven distribution, and soaring cost of Li resources though they are dominant energy storage devices for portable electronics and electric vehicles.^[1] As an alternative, sodium-ion batteries (SIBs) and potassium-ion batteries (PIBs) possess the merits of higher earth abundance of sodium and potassium than lithium^[2] and the capability of using cheaper and lighter Al as the current collector for both anode and cathode. The development of PIBs gains further momentum owing to the commercial availability of graphite anodes, capable of delivering a high and reversible capacity of 278 mAh g⁻¹ for K-ion storage. This is attributed to the formation of KC₈, resulting in a low operating voltage platform at approximately 0.4 V (vs. K⁺/K), whereas the intercalation of Na into graphite is limited to NaC₆₄.^[3] Despite the enormous potential of PIBs, the considerable ionic size of K⁺ (1.33 Å)

typically induces severe volumetric variation during potassiation and depotassiation, leading to structure damage and performance degradation. For graphite, it is subjected to a volume expansion about 60% during potassiation, thereby posing significant challenges to the cycling stability of graphite anode in PIBs.^[4]

Compared with graphite, hard carbon (HC) with the disordered structure possesses larger interlayer spacings with porous structure, which can effectively accommodate the volume variation during potassiation and depotassiation processes. In addition, the heteroatoms modification and large specific surface of HC can offer additional storage sites for K⁺ to improve the specific capacity. In recent years, biomass-derived HCs have garnered significant attention owing to the characteristics of widespread precursor sources, environmental benignity, and cost-effectiveness.^[5] Besides, some biomass sources possess unique internal microstructures, which can be retained after carbonization for effective K⁺ storage.^[6] Despite the above advantages, various impediments such as low initial Coulombic efficiency (ICE), low specific capacity, and poor cycling stability (Table S1)^[5c,7] limit the application of biomass-derived HCs in PIBs.

Among the various biomass precursors, coconut shell stands out as an ideal candidate by virtue of its low ash content (0.61 wt%) and high carbon content.^[8] Coconut shell-derived hard carbon (CS-HC) has been commercialized and reported for SIBs with high ICE and superior electrochemical properties.^[8,9] For example, Wu *et al.*^[9d] reported a CS-HC with an expanded d₍₀₀₂₎-spacing of 0.4 nm for SIBs, which achieved a high ICE of 69.2% and excellent cycling stability (92% capacity retention after 200 cycles). So far, scarce literature exists concerning the utilization of CS-HC as an anode material for PIBs.

[a] Dr. L. Tan, J. Chen, L. Wang, N. Li, Y. Yang, Y. Chen, Prof. L. Guo, Prof. Y. Zhu
Key Laboratory of Bio-Inspired Smart Interfacial Science and Technology, Ministry of Education
School of Chemistry, Beijing Advanced Innovation Center for Biomedical Engineering
Beihang University, Beijing 100191, China
E-mail: yujiezu@buaa.edu.cn

[b] Dr. L. Tan
School of Physics, Beihang University, Beijing 100191, China

[c] Prof. X. Ji
School of Optical and Electronic Information Huazhong University of Science and Technology
Wuhan, Hubei 430074, P. R. China

Supporting information for this article is available on the WWW under <https://doi.org/10.1002/batt.202400010>

In this contribution, we synthesized a CS-HC and investigated its electrochemical performance as an anode material for PIBs. It delivers a reversible specific capacity of 280 mAh g^{-1} at 50 mA g^{-1} with 220 mAh g^{-1} originating from the low potential region ($< 1 \text{ V}$ vs. K^+/K) during depotassiation and more importantly, a high ICE of 87.32% is obtained for present CS-HC, outperforming all previously reported biomass-derived carbon for PIBs (Table S1). It also exhibits sustained long-term cycling stability with 92.8% capacity retention after 100 cycles at 50 mA g^{-1} and rapid potassiation-depotassiation kinetics (280 mAh g^{-1} at 300 mA g^{-1} and 76.2% capacity retention after 500 cycles). Mechanistic insights gained from *ex situ* Raman spectra and cyclic voltammetry test suggest the hybrid charge storage mechanism of CS-HC encompassing (pseudo)capacitive adsorption/desorption of K^+ at active sites at higher voltage and solid-state diffusion-limited intercalation/deintercalation at lower voltage, during which the (pseudo)capacitive behavior plays a dominant role. Finally, a $\text{CS-HC} \mid \text{K}_2\text{Mn}[\text{Fe}(\text{CN})_6](\text{KMF})$ full-cell without precycling either CS-HC anode or KMF cathode is assembled and demonstrates a high capacity retention of 90.6% at 15 mA g^{-1} after 100 cycles and fast rate performance. Considering its low cost, large capacity, high ICE, and stable cycling performance, the present SC-HC shows substantial potential towards practical PIBs.

Results and Discussion

In present study, the CS-HC sample was prepared by a scalable method including the hydrothermal treatment of coconut shell precursor, ball-milling, hydrochloric acid etching, and high-temperature carbonization, as schematically depicted in Scheme 1. In the first step, the fresh coconut shell underwent hydrothermal pretreatment during which the soluble impurities can be effectively removed. Then, the sample was ball-milled and further treated by hydrochloric acid to remove the impurities soluble in acids but insoluble in water. Finally, the CS-HC sample was obtained by a thermal carbonization at 1300°C under Ar atmosphere. The tap density of CS-HC is measured to be around 0.5 g cm^{-3} . Scanning electron microscopy (SEM) and transmission electron microscopy (TEM) were utilized to characterize the morphology and microstructure of the CS-HC sample. The SEM image (Figure 1A) exhibits irregular

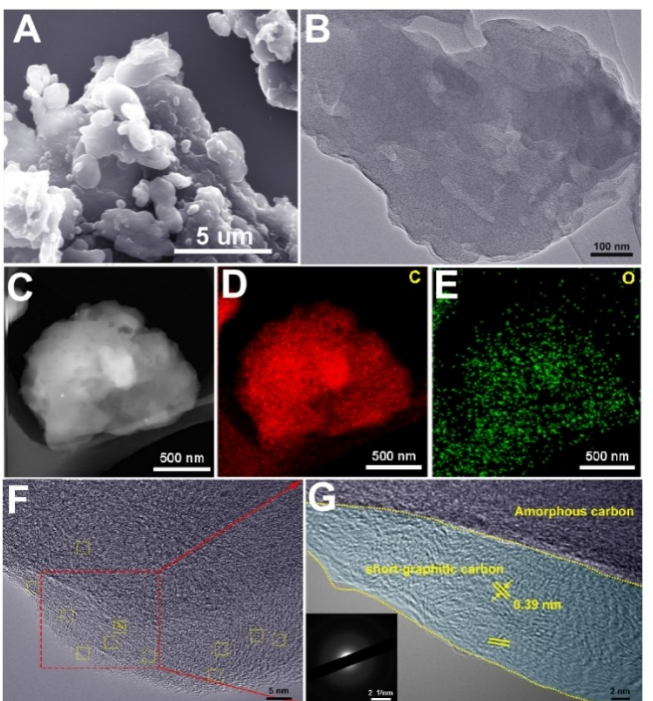
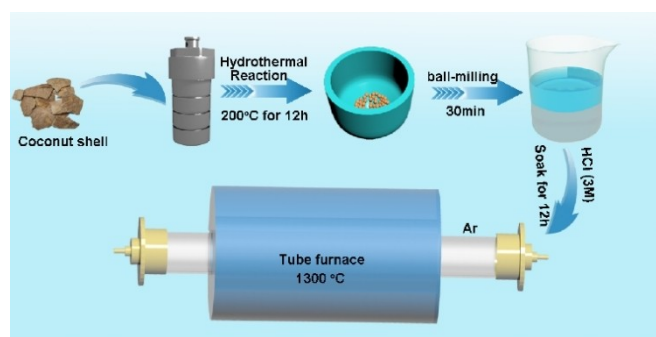


Figure 1. (A) SEM, (B) TEM images of CS-HC, (C–E) TEM image and the corresponding EDS element mapping of C and O, (F, G) HRTEM images of CS-HC. The inset of (G) shows the SAED pattern of CS-HC.



Scheme 1. Schematic illustration of the synthetic pathways of CS-HC.

morphology with small nanoparticles attached to the external surfaces of large particles with several micrometers in size. The TEM image (Figure 1B) displays the dense structure of the CS-HC without obvious pores, in accordance with the surface observed by SEM. Additionally, the TEM energy dispersive X-ray spectroscopy (EDS) elemental mapping images (Figure 1C–E) demonstrate the uniform distribution of C and O elements in the sample with respective element ratios of 98.27 wt% for C and 1.73 wt% for O. Previous studies have demonstrated that the O doping endows HC with abundant surface active sites and an expanded interlayer spacing to boost the K^+ storage capacity and lower the diffusion barrier for K^+ insertion/extraction.^[9d,10] The detailed lattice structure of the CS-HC is further studied via high-resolution TEM (HR-TEM) analysis (Figure 1F, G). The results indicate typical amorphous carbon with short-range graphitic domains which show broken and distorted carbon lattices with estimated lattice fringes of $\sim 0.39 \text{ nm}$. Furthermore, the selected area electron diffraction (SAED) pattern in the inset of figure 1G exhibits only diffuse rings, suggesting the amorphous nature of the CS-HC.

The structure characterization of the sample is conducted using X-ray diffraction (XRD) (Figure 2A). The XRD pattern shows two broad diffraction peaks centered at $2\theta = 22.6^\circ$ and 43.9° , assigned to the (002) and (101) crystal planes of graphitic carbon, respectively. Notably, the (002) peak of the CS-HC has a significant shift towards lower angles in comparison to that of the graphite (26.4° , JCPDS No. 41-1487). This indicates that the CS-HC has a larger d -spacing (0.393 nm) than graphite (0.337 nm as derived by the Bragg equation). The Raman

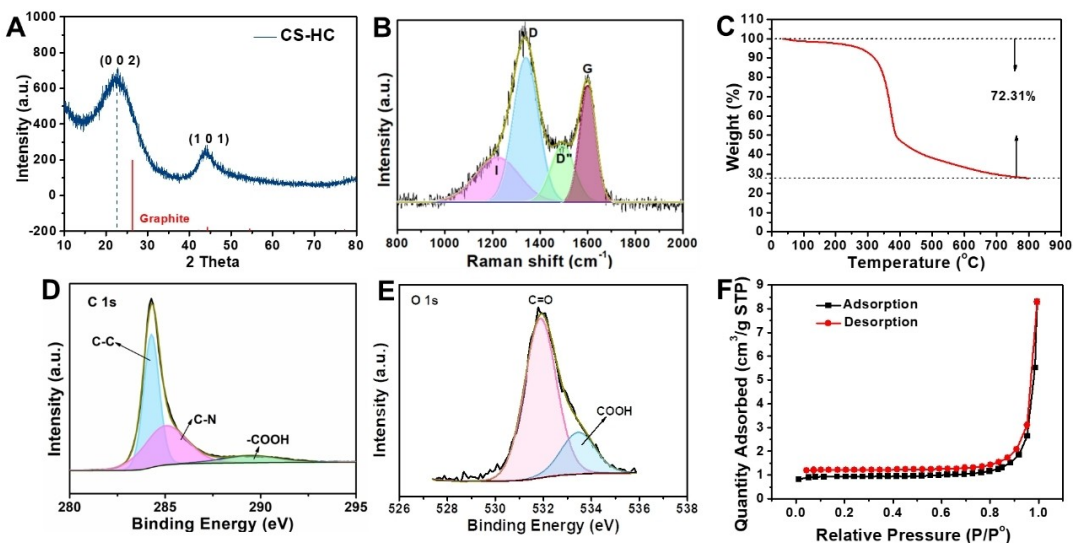


Figure 2. (A) XRD pattern (with the standard (002) diffraction peak of Graphite (JCPDF No 41-1487) presented), (B) Raman spectra, (C) TGA curve, (D) XPS C 1s, (E) O 1s spectra, and (F) N_2 adsorption-desorption isotherms of the CS-HC sample.

spectrum was further obtained to reveal more structural information of the CS-HC. As shown in Figure 2B, it is deconvoluted into four peaks at $\sim 1220\text{ cm}^{-1}$ for I band, $\sim 1339\text{ cm}^{-1}$ for D band, $\sim 1494\text{ cm}^{-1}$ for D'' band, and $\sim 1596\text{ cm}^{-1}$ for G band. The D and G bands are correlated with the breathing modes of disordered carbon atoms or defect characteristics of carbon and the lattice vibration patterns of graphite or the crystallinity of carbon, respectively. The I band is related to the disorder in the graphitic lattice or the existence of polyenes. The D'' band indicates that the amorphous carbon is obtained.^[11] The calculated integral intensity ratio of I_D/I_G is 2.42, demonstrating that the CS-HC is dominated by disordered carbon atoms and defects, consistent with the TEM observations. To investigate the carbonization process, thermogravimetric analysis (TGA) is performed to hydrothermally treated coconut shells in the temperature range of 30–800 °C under Ar atmosphere. As shown in Figure 2C, the sample exhibits a slight weight loss (7.0 wt %) between 30 and 300 °C, corresponding to the volatilization of water and small molecules. The following significant weight loss (51.3 wt %) in the temperature range of 300–450 °C is ascribed to the pyrolysis and carbonization of the main components of coconut shells (lignin, cellulose and carbohydrate).^[12] Subsequently, the weight loss above 450 °C may be due to some dehydrogenation and local graphitization reactions. Based on the TGA result, the carbonization ratio of coconut shell is estimated to be 27.69 wt %. Furthermore, the surface chemistry of the CS-HC sample is characterized by X-ray photoelectron spectroscopy (XPS). XPS survey spectra demonstrates that the sample consists of only C and O (Figure S1). The high-resolution XPS spectrum of C 1s shown in Figure 2D can be deconvoluted into three peaks centered at 284.4, 285.3 and 289.68 eV, corresponding to C–C, C–N, and –COOH bonds, respectively. Moreover, the O 1s signal (Figure 2E) can be fitted with two contributions with binding energies located at 531.8 and 533.6 eV, which are attributed to C=O and COOH bonds,

respectively.^[11a,13] Then, N_2 adsorption-desorption analysis is employed to investigate the surface area and pore size distribution of the sample. Figure 2F presents type-II isotherm curves, indicating the nonporous or macroporous structure of the sample (Figure S2), consistent with the TEM results. Notably, the sample possesses a small Brunauer–Emmett–Teller (BET) surface area of $3.72\text{ m}^2\text{ g}^{-1}$, which can reduce its contact area with the electrolyte, mitigating the irreversible capacity loss from the formation of solid electrolyte interphase (SEI) to achieve high ICE.

Next, the electrochemical performance of the CS-HC is evaluated in the K metal half-cells within the potential range of 0.01–3 V (vs. K^+/K). Unless otherwise specified, potentials are referenced to K metal in the following discussion. Figure 3A shows the cyclic voltammetry (CV) curves of the CS-HC at the scanning rate of 0.1 mV s^{-1} . The first cycle contains two cathodic peaks and one anodic peak. The small and broad cathodic peak around 0.78 V, which disappears in the subsequent cycles, is related to the decomposition of the electrolyte to form the SEI film on the electrode. This indicates that the side reaction mainly occurs in the first cycle. The large and sharp cathodic peak observed in the low-potential region at 0.02 V is rooted in the potassiation of the CS-HC^[4,14] and the anodic peak at 0.53 V is assigned to the corresponding depotassiation process. The galvanostatic potassiation-depotassiation curves at 50 mA g^{-1} are shown in Figure 3B. The CS-HC delivers initial specific potassiation and depotassiation capacities of 329.5 and 287.7 mAh g^{-1} , respectively, alongside a notable high ICE of 87.32%. In the following cycles, a highly reversible specific capacity of 280 mAh g^{-1} is achieved and the CE reaches 99.3% after the third cycle, indicating the good reversibility of the CS-HC towards K-ion storage. Particularly, a substantial portion of the specific capacity ($\sim 220\text{ mAh g}^{-1}$) comes from the low voltage region ($< 1\text{ V}$) during depotassiation, advantageous for achieving high discharge voltage in full-cell applications. In

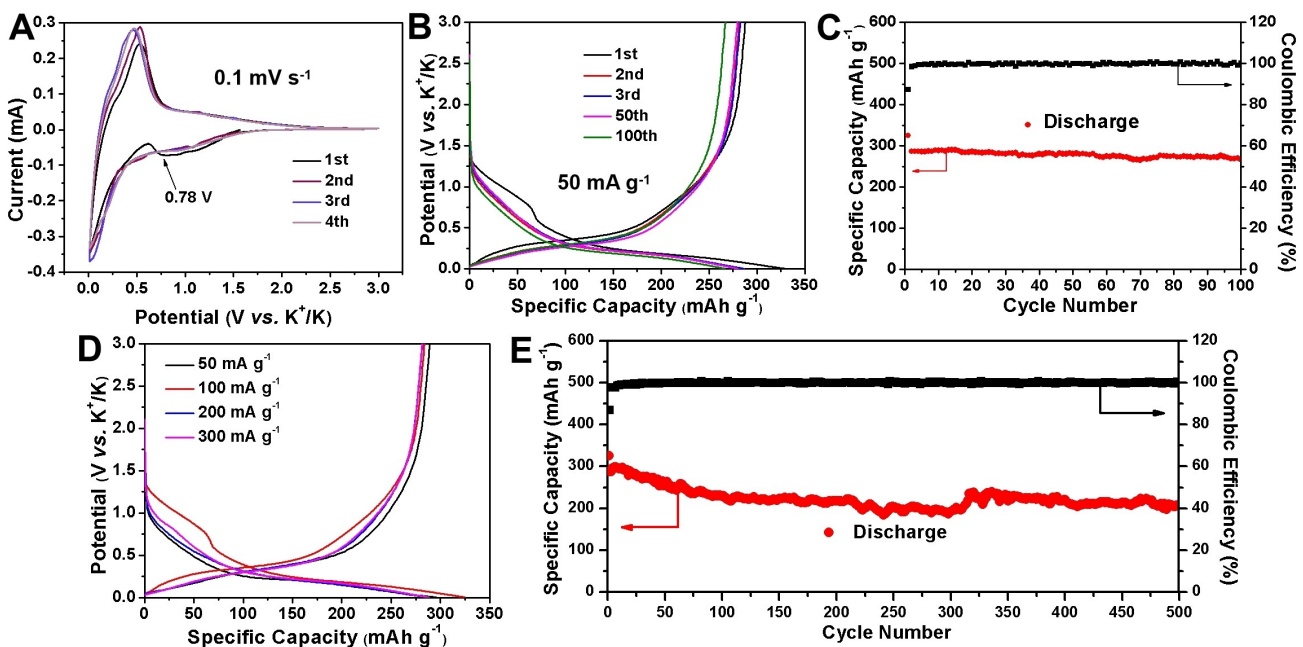


Figure 3. (A) CV profiles of CS-HC at 0.1 mV s^{-1} in the potential range of $0.01\text{--}3 \text{ V}$ during the initial 4 cycles, (B) galvanostatic charge-discharge curves and (C) cycling performance of CS-HC at 50 mA g^{-1} , (D) rate performance of CS-HC, and (E) cycling performance of CS-HC at 300 mA g^{-1} .

contrast, the CS-HC electrode without any pretreatment (Figure S3) delivers an initial depotassiation capacity of 189.5 mAh g^{-1} with an ICE of 70.8%, considerably lower than that of CS-HC with pretreatment, which indicates that the existence of impurity can adversely affect the electrochemical properties of CS-HC. The cycling performance of the CS-HC anode at 50 mA g^{-1} is shown in Figure 3C. After 100 cycles, a reversible capacity of 267.1 mAh g^{-1} is still obtained for the CS-HC, corresponding to a capacity retention of 92.8% in comparison to the initial depotassiation capacity, and the average CE is as high as 99.3%. Rate capability test (Figure 3D) is further carried out to assess the kinetic characteristics of the CS-HC. When the current density is increased from 50 mA g^{-1} to 300 mA g^{-1} , the reversible capacity only changes from $287.7 \text{ to } 280 \text{ mAh g}^{-1}$, indicating the fast K-ion storage reaction kinetics of the sample. As shown in Figure 3D, when the specific current experiences a 6-fold increase from 50 mA g^{-1} to 300 mA g^{-1} , the charge-discharge curves exhibit similar shape with only a slightly increased overpotential of 0.185 V , highlighting the rapid reaction kinetics of the CS-HC. Finally, the long-term cycling stability of the CS-HC is tested at 300 mA g^{-1} and the result shows that it can still offer a specific capacity of 213.5 mAh g^{-1} after 500 cycles (corresponding to 76.2% capacity retention), demonstrating its superior long-term cycling performance (Figure 3E, S4).

To gain insight into the potassium storage mechanism, the *ex situ* Raman measurements are applied to monitor the structural evolutions of the CS-HC at different states of potassiation/depotassiation (Figure 4). No obvious shift of the D and G bands position is observed until discharge (potassiation) to 0.26 V (point A–C in Figure 4B, C) and meanwhile, the integrated density ratio of I_D/I_G only slightly decreases, indicat-

ing that the charge storage predominantly originates from the surface adsorption on defects or active sites, consistent with previous reports.^[15] Subsequently, a sharp decrease in the I_D/I_G ratio is noted upon discharge to 0.01 V (point D in Figure 4C), demonstrating the increased degree of structural ordering. This is probably attributed to the K-ion insertion into the interlayers of CS-HC, as reported in the literature which demonstrated that alkali metal ions insertion can induce localized crystallization of HC.^[7d] In the charge (depotassiation) process, the I_D/I_G shows slow recovery, revealing the good reversibility of the electrochemical reactions. Notably, at the end of charge, the I_D/I_G still deviates from the value of the pristine state probably because of the formation of SEI. The evolution of the *ex situ* Raman spectra clearly indicates the hybrid potassium storage behaviors involving ion adsorption and intercalation.

Then, cyclic voltammetry test with increasing scan rates from 0.05 to 0.4 mV s^{-1} is performed to further semi-quantitatively investigate the capacity contribution ratio between the surface (pseudo)capacitance and bulk diffusion behaviors (Figure S5). As shown in Figure S5A, with the increase of scanning rate, both the anodic and cathodic peaks barely change their shapes and the peak potentials almost maintain constant values, indicating the fast reaction kinetics of the CS-HC towards K-ion storage. As reported in the literature, the relationship between the current response (i) under a certain voltage and the scan rate (v) conforms to the following equation:^[16]

$$i = av^b \quad (1)$$

where a and b are constants and the value of b ranges from 0.5 to 1 , corresponding to complete solid-state diffusion-controlled

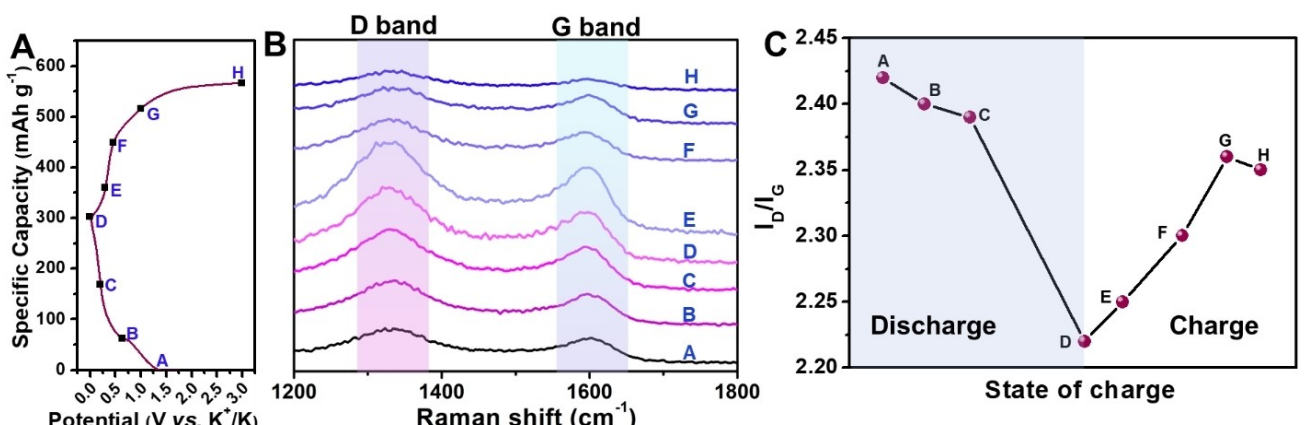


Figure 4. (A) Galvanostatic charge-discharge curve and (B) *ex situ* Raman spectra of CS-HC in the initial cycle at the current density of 50 mAh g⁻¹, (C) The integrated density ratio of I_D/I_G at different states of potassiation/depotassiation.

Faradaic insertion process ($b=0.5$) and (pseudo)capacitive contribution ($b=1$), respectively. The value of b can be calculated from the slope from the following equation (2)

$$\log i = \log a + b \log v \quad (2)$$

As displayed in Figure S5B, the b values are estimated to be 0.8559 and 0.8764 from the cathodic peak at 0.1 V and anodic peak at 0.3 V, suggesting that the charge storage involves both the surface (pseudo)capacitive and bulk diffusion behaviors. The corresponding b values at various potentials are further obtained, which range from 0.8 to 1 (Figure S5C), suggesting that the current is mainly dominated by the (pseudo)capacitive behavior. To further quantitatively estimate the proportion of both contributions, Equation (1) can be re-written as:

$$i = k_1 v + k_2 v^{1/2} \quad (3)$$

where the $k_1 v$ and $k_2 v^{1/2}$ refer to the capacitance and the Faraday effect's current response, respectively,^[17] which can be distinguished by plotting the $i/v^{1/2}$ vs. $v^{1/2}$ by rearranging equation 3 to equation 4 as following:

$$i/v^{1/2} = k_1 v^{1/2} + k_2 \quad (4)$$

Taking the CV curve of 0.05 mVs⁻¹ as an example (Figure S5D), at the cathodic peak of 0.1 V and anodic peak of 0.4 V, the (pseudo)capacitive contribution to the current is 62.4% and 51.9%, respectively. For the other potentials, the (pseudo)capacitive contribution is over 60%, suggesting that the charge storage is mainly dominated by the (pseudo)capacitive behavior, which explains the fast rate capability observed in Figure 3D.

Compared with graphite, the larger interlayer distance of the CS-HC is expected to alleviate the volume changes of anode during K-ion storage. To assess the practical application of the CS-HC, the thickness variation of the CS-HC electrode is measured during repeated potassiation and depotassiation. To make a practical relevance assessment and accurately measure

the thickness change of the electrode, a high loading mass of 10 mg cm⁻² CS-HC is used. Figure S6 displays the electrochemical potassiation-depotassiation performance of the high-loading electrode. As shown in Figure S6, under a loading of 10 mg cm⁻², the CS-HC can provide a specific capacity of 260 mAh g⁻¹, close to the value obtained in Figure 3B, and an areal capacity of 2.48 mAh cm⁻² is obtained, which is in line with the parameter in contemporary LIBs. As depicted in Figure S7, the CS-HC electrode swells during potassiation and shrinks upon subsequent depotassiation. The maximum swelling ratio during the initial 3 potassiation-depotassiation cycles is 5.3 vol%, smaller than that of graphite electrode,^[14a,18] demonstrating the feasibility of utilizing the CS-HC in practical PIBs. Such a small swelling ratio is attributed to the large d -spacing of present CS-HC and the surface pseudocapacitive charge storage mechanism. During the 4th cycle, the swelling ratio during the potassiation becomes smaller and the thickness variation between potassiation and depotassiation is reduced, implying the attainment of a steady state.

Furthermore, a full-cell consisting of the high-voltage KMF cathode and CS-HC anode is assembled and tested to evaluate the practical feasibility of the CS-HC anode in PIBs (Figure 5A). The capacity ratio of the positive electrode: negative electrode is set to be 1:1.1 for the full-cell to avoid potassium metal deposition. Different from most previously published works in which either cathode or anode, occasionally both, was precycled in the K metal cells before assembling the full-cells,^[19] the CS-HC || KMF full-cell is directly assembled with pristine CS-HC anode and KMF cathode, capitalizing on the high ICE of the CS-HC anode. The galvanostatic charge-discharge curves of the full-cell tested at 0.1 C (1 C = 150 mAh g⁻¹, calculated on the basis of the mass of KMF in the full-cell) in the voltage range of 0–4.3 V are shown in Figure 5B. The full-cell displays a sloped discharge curve with an average discharge voltage of 2.8 V and a stable discharge capacity of 74 mAh g⁻¹. As shown in Figure 5C, the CS-HC || KMF full-cell sustains a specific discharge capacity of 70 mAh g⁻¹ even after 100 cycles, corresponding to 90.6% capacity retention in comparison to the 1st cycle, which demonstrates the good stability of the full-cell. Meanwhile,

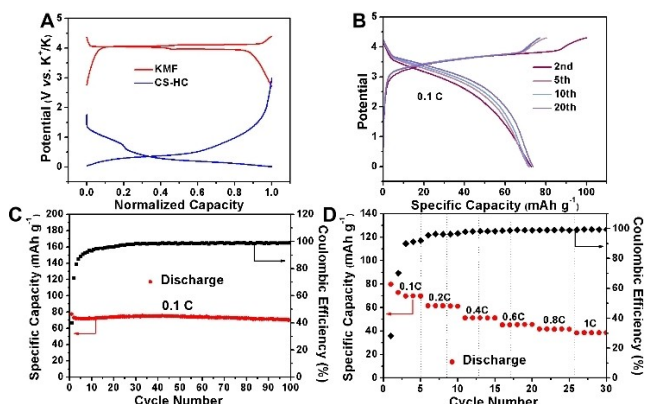


Figure 5. (A) Normalized galvanostatic charge-discharge curves of KMF cathode and CS-HC anode. (B) galvanostatic charge-discharge curves, (C) cycling performance, and (D) rate performance of CS-HC//KMF full-cell.

voltage profiles (Figure 5B) display consistent shapes without observable polarization escalation during cycling. In addition, the CE of the full-cell consistently increases in the initial few cycles and the average CE of the full-cell is over 99.0% after 30 cycles. Besides the stable cycling performance, the full-cell also shows fast rate performance (Figure 5D, S8). Specifically, it exhibits reversible specific capacities of 70, 62, 52, 46, 42, and 39 mAh g⁻¹ at the specific currents of 0.1, 0.2, 0.4, 0.6, 0.8, and 1 C, respectively, demonstrating the outstanding electrochemical stability of the full-cell.

Conclusions

In summary, we have successfully synthesized a high-performance HC anode suitable for PIBs from low-cost coconut shell. The CS-HC displays a large interlayer spacing of 0.393 nm with a low specific area of 3.72 m² g⁻¹, which is conducive to K-ion storage and effectively reduce the side reactions between the CS-HC and electrolyte. Hence, the CS-HC anode exhibits a high K-ion storage specific capacity of 287.7 mAh g⁻¹ (with 220 mAh g⁻¹ obtained below 1 V during depotassiation) and an impressive ICE of 87.32%. Moreover, it exhibits commendable rate capability with a specific capacity of 280 mAh g⁻¹ at 300 mA g⁻¹ and good long-term cycling stability with 76.2% capacity retention after 500 cycles. Mechanistic studies from the *ex situ* Raman spectra demonstrate the hybrid charge storage mechanisms encompassing (pseudo)capacitive behavior and solid-state intercalation-deintercalation during potassiation/depotassiation. The cyclic voltammetry test further demonstrates that the K-ion storage capacity is mainly dominated by (pseudo)capacitive behavior contribution. Finally, a full-cell consisting of unrecycled CS-HC anode and KMF cathode presents an average discharge voltage of 2.8 V and retains 90.6% of initial capacity after 100 charge-discharge cycles. Given the merits of low-cost precursor, scalable synthesis procedure, high ICE, and low working voltage, the proposed hard carbon holds substantial promise for practical PIBs.

Supporting Information

The authors have cited additional references within the Supporting Information.^[20,21]

Acknowledgements

We acknowledge the financial support from the National Natural Science Foundation of China (52172177 and 5237011592).

Conflict of Interests

The authors declare no conflict of interest.

Data Availability Statement

The data that support the findings of this study are available from the corresponding author upon reasonable request.

Keywords: Potassium-ion batteries • Anode materials • Hard carbon • Biowaste

- [1] a) Y. Sun, N. Liu, Y. Cui, *Nat. Energy* **2016**, *1*, 16071; b) S. K. Heiskanen, J. Kim, B. L. Lucht, *Joule* **2019**, *3*, 2322–2333; c) J.-M. Tarascon, *Nat. Chem.* **2010**, *2*, 510; d) J.-M. Tarascon, M. Armand, *Nature* **2001**, *414*, 359–367.
- [2] a) L. Deng, T. Wang, Y. Hong, M. Feng, R. Wang, J. Zhang, Q. Zhang, J. Wang, L. Zeng, Y. Zhu, *ACS Energy Lett.* **2020**, *5*, 1916–1922; b) R. Zhou, H. Tan, Y. Gao, Z. Hou, X. Du, B. Zhang, *Carbon* **2022**, *186*, 141–149.
- [3] R. C. Asher, S. A. Wilson, *Nature* **1958**, *181*, 409–410.
- [4] W. Luo, J. Wan, B. Ozdemir, W. Bao, Y. Chen, J. Dai, H. Lin, Y. Xu, F. Gu, V. Barone, L. Hu, *Nano Lett.* **2015**, *15*, 7671–7677.
- [5] a) B. Lu, C. Lin, H. Xiong, C. Zhang, L. Fang, J. Sun, Z. Hu, Y. Wu, X. Fan, G. Li, J. Fu, D. Deng, Q. Wu, *Molecules* **2023**, *28*, 4027; b) L.-J. Xie, C. Tang, M.-X. Song, X.-Q. Guo, X.-M. Li, J.-X. Li, C. Yan, Q.-Q. Kong, G.-H. Sun, Q. Zhang, F.-Y. Su, C.-M. Chen, *J. Energy Chem.* **2022**, *72*, 554–569; c) S. Chen, K. Tang, F. Song, Z. Liu, N. Zhang, S. Lan, X. Xie, Z. Wu, *Nanotechnology* **2021**, *33*, 55401.
- [6] a) Y. Shen, S. Sun, M. Yang, X. Zhao, *J. Alloys Compd.* **2019**, *784*, 1290–1296; b) E. Hao, W. Liu, S. Liu, Y. Zhang, H. Wang, S. Chen, F. Cheng, S. Zhao, H. Yang, *J. Mater. Chem. A* **2017**, *5*, 2204–2214.
- [7] a) T. Huang, D. Peng, Z. Chen, X. Xia, Y. Chen, H. Liu, *New Carbon Mater.* **2022**, *37*, 1125–1132; b) X. Zhang, R. Huang, F. Wu, R. Chen, L. Li, *Nano Energy* **2023**, *117*, 108913; c) M. Kim, L. Ma, Z. Li, W. Mai, N. Amiralian, A. E. Rowan, Y. Yamauchi, A. Qin, R. A. Afzal, D. Martin, A. K. Nanjundan, J. Li, *J. Mater. Chem. A* **2023**, *11*, 16626–16635; d) X. Yuan, B. Zhu, J. Feng, C. Wang, X. Cai, R. Qin, *Mater. Res. Bull.* **2021**, *139*, 111282.
- [8] M. Thenappan, S. Rengapillai, S. Marimuthu, *Energies* **2022**, *15*, 8086.
- [9] a) Y. Cheng, J. Zhao, L. Zhang, J. Wan, J. Yang, H. Wang, *Solid State Ionics* **2023**, *402*, 116374; b) R. R. Gaddam, D. Yang, R. Narayan, K. Raju, N. A. Kumar, X. S. Zhao, *Nano Energy* **2016**, *26*, 346–352; c) C. Nita, B. Zhang, J. Dentzer, C. M. Ghimbeu, *J. Energy Chem.* **2021**, *58*, 207–218; d) F. Wu, L. Liu, Y. Yuan, Y. Li, Y. Bai, T. Li, J. Lu, C. Wu, *ACS Appl. Mater. Interfaces* **2018**, *10*, 27030–27038.
- [10] Z. Song, M. Di, S. Chen, Y. Bai, *Chem. Eng. J.* **2023**, *470*, 144237.
- [11] a) J. Tu, H. Tong, X. Zeng, S. Chen, C. Wang, W. Zheng, H. Wang, Q. Chen, *Adv. Funct. Mater.* **2022**, *32*, 2204991; b) X. Chen, N. Sawut, K. Chen, H. Li, J. Zhang, Z. Wang, M. Yang, G. Tang, X. Ai, H. Yang, *Energy Environ. Sci.* **2023**, *16*, 4041–4053; c) Y. Liu, S. Wang, X. Sun, J. Zhang, F. uz Zaman, L. Hou, C. Yuan, *Energy Environ. Mater.* **2023**, *6*, e12263; d) M. Ayania, E. Weiss-Hortala, M. Smith, J.-S. McEwen, M. Garcia-Perez, *Carbon* **2020**, *167*, 559; e) J. Zhang, D. Wu, Q. Zhang, A. Zhang, J. Sun, L. Hou, C. Yuan, *J. Mater. Chem. A* **2022**, *10*, 2932.

- [12] M. Yang, Q. Kong, W. Feng, W. Yao, *Carbon* **2021**, *176*, 71–82.
- [13] C. Lu, Z. Sun, L. Yu, X. Lian, Y. Yi, J. Li, Z. Liu, S. Dou, J. Sun, *Adv. Energy Mater.* **2020**, *10*, 2001161.
- [14] a) Z. Jian, W. Luo, X. Ji, *J. Am. Chem. Soc.* **2015**, *137*, 11566–11569; b) J. Yang, Z. Ju, Y. Jiang, Z. Xing, B. Xi, J. Feng, S. Xiong, *Adv. Mater.* **2018**, *30*, 1700104.
- [15] a) Z. Yu, Q. Liu, C. Chen, Y. Zhu, B. Zhang, *J. Power Sources* **2023**, *557*, 232592; b) S. Huang, Z. Li, B. Wang, J. Zhang, Z. Peng, R. Qi, J. Wang, Y. Zhao, *Adv. Funct. Mater.* **2018**, *28*, 1706294.
- [16] X. Luo, W. Li, H. Liang, H. Zhang, K. Du, X. Wang, X. Liu, J. Zhang, X. Wu, *Angew. Chem. Int. Ed.* **2022**, *134*, e202117661.
- [17] J. Wang, J. Polleux, J. Lim, B. Dunn, *J. Phys. Chem. C* **2007**, *111*, 14925–14931.
- [18] a) D. A. Gribble, Z. Li, B. Ozdogru, E. McCulfor, Ö. Ö. Çapraz, V. G. Pol, *Adv. Energy Mater.* **2022**, *12*, 2103439; b) J. Zhao, X. Zou, Y. Zhu, Y. Xu, C. Wang, *Adv. Funct. Mater.* **2016**, *26*, 8103–8110.
- [19] a) W. Xu, H. Li, X. Zhang, T. Chen, H. Yang, H. Min, X. Shen, H. Chen, J. Wang, *Adv. Funct. Mater.* **2023**, *23*09509; b) J. Chen, D. An, S. Wang, H. Wang, Y. Wang, Q. Zhu, D. Yu, M. Tang, L. Guo, H. Wang, *Angew. Chem. Int. Ed.* **2023**, *62*, e202307122; c) X. Yin, Y. Zhao, X. Wang, X. Feng, Z. Lu, Y. Li, H. Long, J. Wang, J. Ning, J. Zhang, *Small* **2022**, *18*, 2105568.
- [20] L. Deng, J. Qu, X. Niu, J. Liu, J. Zhang, Y. Hong, M. Feng, J. Wang, M. Hu, L. Zeng, Q. Zhang, L. Guo, Y. Zhu, *Nat. Commun.* **2021**, *12*, 2167.
- [21] Y. Yao, N. Yao, X. Zhou, Z. Li, X. Yue, C. Yan, Q. Zhang, *Adv. Mater.* **2022**, *34*, 2206448.

Manuscript received: January 10, 2024

Revised manuscript received: January 30, 2024

Accepted manuscript online: January 30, 2024

Version of record online: February 23, 2024